Flexible, Highly Graphitized Carbon Aerogels Based on Bacterial Cellulose/Lignin: Catalyst-Free Synthesis and its Application in Energy Storage Devices

Xuezhu Xu, Jian Zhou, D. H. Nagaraju, Long Jiang, Val R. Marinov, Gilles Lubineau,* Husam N. Alshareef, and Myungkeun Oh*

Currently, most carbon aerogels are based on carbon nanotubes (CNTs) or graphene, which are produced through a catalyst-assisted chemical vapor deposition method. Biomass based organic aerogels and carbon aerogels, featuring low cost, high scalability, and small environmental footprint, represent an important new research direction in (carbon) aerogel development. Cellulose and lignin are the two most abundant natural polymers in the world, and the aerogels based on them are very promising. Classic silicon aerogels and available organic resorcinol–formaldehyde (RF) or lignin–resorcinol–formaldehyde (LRF) aerogels are brittle and fragile; toughening of the aerogels is highly desired to expand their applications. This study reports the first attempt to toughen the intrinsically brittle LRF aerogel and carbon aerogel using bacterial cellulose. The facile process is catalyst-free and cost-effective. The toughened carbon aerogels, consisting of blackberry-like, core–shell structured, and highly graphitized carbon nanofibers, are able to undergo at least 20% reversible compressive deformation. Due to their unique nanostructure and large mesopore population, the carbon materials exhibit an areal capacitance higher than most of the reported values in the literature. This property makes them suitable candidates for flexible solid-state energy storage devices. Besides energy storage, the conductive interconnected nanoporous structure can also find applications in oil/water separation, catalyst supports, sensors, and so forth.

1. Introduction

Aerogels, a family of 3D nanostructured porous materials characterized by low density, large porosity, high specific surface area, and low thermal conductivity, have been used in a broad range of important applications. While silica aerogels prepared by CO_2 supercritical drying are the most classic aerogels, carbon aerogels have attracted increasing research attention in recent years due to their great potential in applications such as supercapacitors,[1] gas sensors,[2] absorbents,[3] and catalyst supports.[4] Current carbon aerogel research is mainly focused on novel precursors, drying methods, nanostructures, and mechanical property improvements (especially toughness) of the aerogels.[5]

Regarding the novel precursors, biomass such as coconut shells,[6] cellulose,[7–10] and lignin[11] have drawn great interest because of their renewability, low cost, and nontoxicity. Lignin as an abundant carbon-rich biopolymer comprises three different phenolic alcohol monomers linked together by C—C or C—O—C linkages to form a 3D polymer network. Although lignin contains phenolic hydroxyl groups, its reactivity is low compared to resorcinol due to high substitution on its benzene rings and the steric hindrance caused by its complex molecular structure. Still, lignin has been used to partially substitute resorcinol in producing lignin–resorcinol–formaldehyde (LRF) aerogels through freeze–drying[12] and freeze–thaw–drying.[13] The aerogels exhibit a network structure of interconnected zero-dimensional

X. Xu, Prof. L. Jiang, M. Oh
Department of Mechanical Engineering
North Dakota State University
Fargo, ND 58102, USA
E-mail: long.jiang@ndsu.edu

X. Xu, Prof. L. Jiang, M. Oh
Program of Materials and Nanotechnology
North Dakota State University
Fargo, ND 58102, USA

Dr. J. Zhou, Prof. G. Lubineau
COHMAS Laboratory, Physical Science and Engineering Division
King Abdullah University of Science and Technology (KAUST)
Thuwal 23955-6900, Saudi Arabia
E-mail: gilles.lubineau@kaust.edu.sa

DOI: 10.1002/adfm.201500538

Dr. D. H. Nagaraju, Prof. H. N. Alshareef
Physical Science and Engineering Division
King Abdullah University of Science and Technology (KAUST)
Thuwal 23955-6900, Saudi Arabia

Prof. V. R. Marinov
Department of Industrial and Manufacturing Engineering
North Dakota State University
Fargo, ND 58102, USA

nanoaggregates, which form numerous 15–30 nm mesopores inside the aerogels. Lignin–phenol–formaldehyde,[14] lignin–tannin,[15] and lignin–cellulose[16,17] aerogels have also been synthesized using similar techniques.

Cellulose, synthesized by plants, algae, and bacteria, is the most abundant natural polymer on the earth. Bacterial cellulose (BC) gels are produced by bacteria *gluconacetobacter xylinus* in culture and they comprise high-crystallinity (up to 90%), ultrafine (5–50 nm) cellulose nanofibers. BC nanofibers share many properties of plant-based cellulose nanofibers, including outstanding mechanical properties, rich surface chemistry, nontoxicity, biocompatibility, and high transparency (in films). However, BC in general is considered superior to the plant-based cellulose nanofibers because they are of higher crystallinity and free of lignin/semicellulose and their production requires no harsh chemical/mechanical treatments. As a traditional dessert in Southeast Asia, BC is readily available at low cost. BC gels have been converted into aerogels through freeze–drying, which are then used as templates to grow other nanomaterials such as anatase nanowires[18] and magnetic nanoparticles.[19] BC-based aerogels have further been converted into carbon aerogels through pyrolysis, which exhibits high mechanical flexibility, outstanding fire resistance, and strong adsorption capability.[20]

The fragility of the lignin-based aerogels, which originate from the interconnected nanoaggregates inside the gels, is the main drawback of these innovative products and therefore has limited their applications.[21] The main goal of this study is to develop flexible lignin-based aerogels and carbon aerogels. For the first time, both gels are toughened using BC as a scaffold. BC is impregnated with LRF solution and BC–LRF hydrogels are obtained through polycondensation of LRF. BC–LRF aerogels and carbon aerogels are subsequently produced using CO_2 supercritical drying and catalyst-free carbonization. The obtained carbon aerogels exhibit a unique blackberry-like nanostructure and their mechanical behavior is similar to that of CNTs- or graphene-based carbon sponges, which are generally synthesized by catalyst-assisted growing processes.[3,22,23] Catalyst-free synthesis is a more cost-effective and environment-friendly process and the obtained carbons need no further treatments for catalyst removal. The blackberry-like structure, with the BC-converted carbon nanofibers as the backbone and the LRF-converted carbon nanoaggregates as the blackberry-like coating, shows modest surface areas but surprisingly high areal capacitance. This high value is due to the highly conductive BC carbon fiber network and the porous "blackberry" surface suitable for ion storage.

2. Results and Discussion

2.1. Formation of Lignin–Resorcinol–Formaldehyde Hydrogels

Lignin molecules contain reactive sites similar to those of phenol/resorcinol (i.e., ortho, meta, and para carbons on the benzene rings) and hence they have been used to partially replace phenol/resorcinol to produce organic hydrogels and aerogels using formaldehyde as the crosslinker.[14,24] During gelation, formaldehyde first reacts with phenol/resorcinol and lignin to form hydroxymethyl (—CH_2OH) derivatives of the three chemicals, which subsequently form methylene (–CH_2–) and methylene ether (–CH_2OCH_2–) bridged gel networks through condensation (**Figure 1**A).[25,26] Figure 1B shows the Fourier transform infrared spectroscopy (FTIR) spectra of dried LRF gel powder, where the additional peaks at 1473.3 and 1087.7 cm^{-1} are associated with –CH_2 and C—O bending vibrations of benzyl ether linkages,[14] confirming the successful formation of the gel network. The effect of the L:R:F ratio on the gel property is shown in the ternary plot in Figure 1C. Rigid gels (LRF9 and LRF10) are formed at low lignin concentrations;

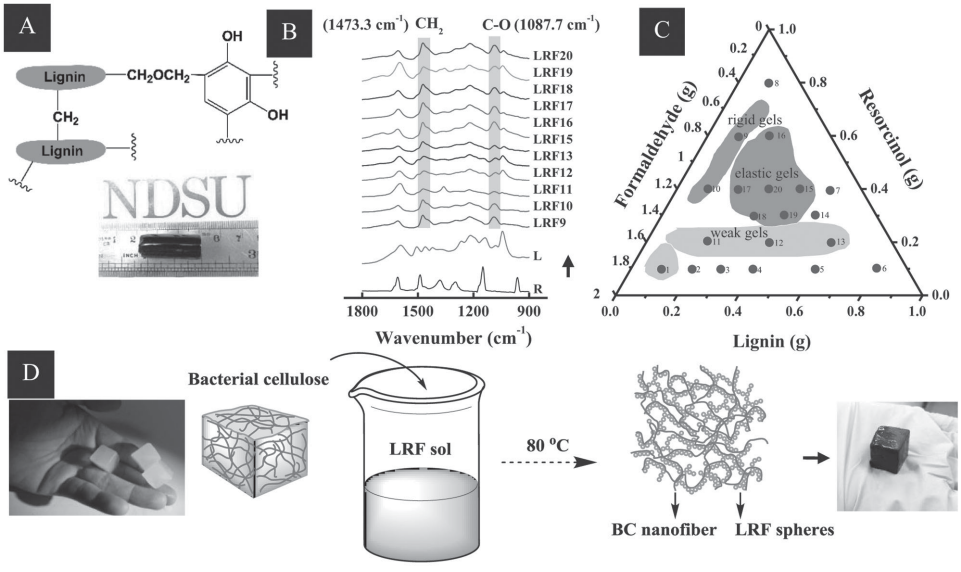

Figure 1. A) Schematic macromolecular structure of an LRF hydrogel and an LRF16 hydrogel sample. B) FTIR spectra of dried LRF gel powder. C) Ternary plot of the gel property of various LRF hydrogels (refer to Table 4 for the formulation of each sample). D) Process to produce BC–LRF hydrogel.

weak gels (LRF1, 11, 12, and 13) are formed when the resorcinol concentration is low; strong elastic gels are obtained for samples LRF15, 16, 17, 18, 19, and 20, which are all located in the central region of the triangle. The rest of the samples show no sign of gelation. All the hydrogels exhibit similar densities (≈0.8 g cm^{-3}) and water contents (≈80%), suggesting that the different strengths/modulus of the gels are mainly due to their varying crosslinking densities. Lignin has less reactive sites and higher steric hindrance compared to phenol/resorcinol because its aromatic rings are highly substituted.[14] Therefore, a low resorcinol concentration means reduced reactive carbons available for the reactions with formaldehyde, causing low crosslinking density and low gel strength/modulus. At low lignin concentrations, there are plenty of resorcinol and formaldehyde to react to form highly crosslinked hard gels. To achieve the gels with high lignin concentration and high gel strength, lower molecular weight lignin (e.g., partially depolymerized lignin or low molecular weight lignin fraction) that has higher number of approachable reactive sites can be used.

2.2. Formation and Microstructure of BC–LRF Carbon Aerogels

After the formulation–gelation behavior relationship was determined, the L:R:F ratios that yielded elastic hydrogels were chosen to synthesize BC–LRF carbon aerogels. BC–LRF hydrogels were first obtained by crosslinking the LRF, which was impregnated into BC (Figure 1D) and the products were subsequently dried using supercritical CO_2 to produce BC–LRF aerogels. For comparison pure BC and LRF hydrogels were

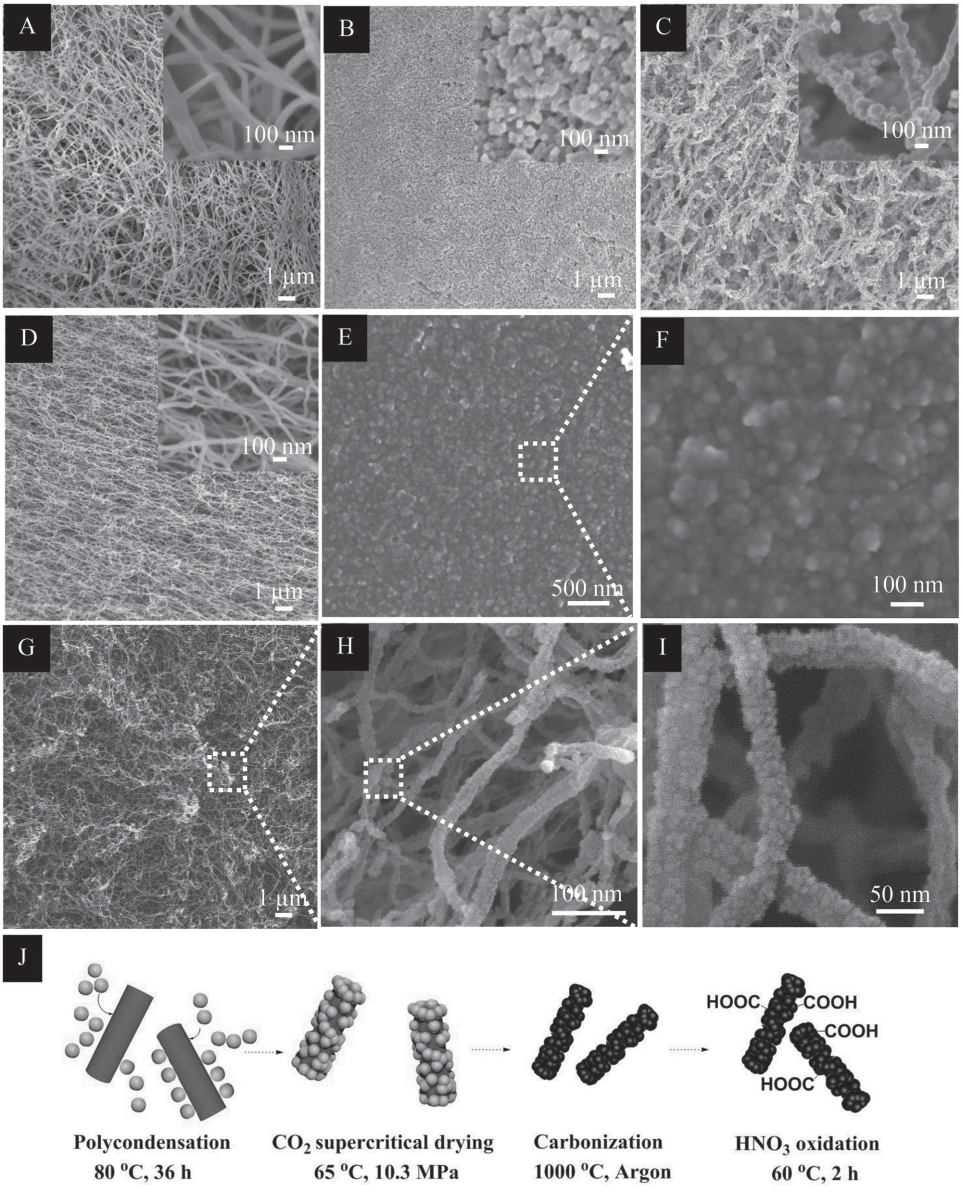

Figure 2. SEM images of A) BC aerogel; B) LRF16 aerogel; C) BC–LRF16 aerogel; D) BC carbon aerogel; E,F) LRF16 carbon aerogel; G–I) BC–LRF16 carbon aerogel; J) Microstructure evolution of the BC–LRF carbon aerogel.

Table 1. Sizes of the nanofibers or nanoaggregates in BC, LRF, and BC–LRF aerogels and carbon aerogels.

Material	Mean diameter [nm]	Standard deviation [nm]	Shape
BC aerogel	69.0	24.5	Continuous fiber
LRF aerogel	59.0	8.2	Aggregate
BC–LRF aerogel	128.3	47.1	Continuous fiber
BC carbon aerogel	25.6	4.7	Continuous fiber
LRF carbon aerogel	57.9	16.2	Aggregate
BC–LRF carbon aerogel	41.1	6.6	Continuous fiber

also converted into aerogels using the same drying conditions. Scanning electron microscopy (SEM) images of the BC, LRF, and BC–LRF aerogels are compared in **Figure 2**. BC nanofibers (Figure 2A) and LRF nanoaggregates (Figure 2B) can be clearly seen in their respective aerogels. In the BC–LRF aerogel, the LRF nanoaggregates were decorated on the surface of the BC nanofibers to form a blackberry-like hierarchical structure (Figure 2C). The diameter of the BC nanofibers is almost doubled due to the decoration (**Table 1**). The carbon aerogels converted from the above aerogels are shown in Figure 2D–I. The carbonization process preserves the structure of the aerogels although it significantly reduces the size of the nanofibers and nanoaggregates (Table 1). The BC–LRF carbon aerogel has an average diameter of 41.1 nm and the fibers are continuous. The evolution of the blackberry-like structure from the hydrogel to the carbon aerogel is illustrated in Figure 2J.

Transmission electron microscopy (TEM) images of the BC and BC–LRF carbon aerogels are compared in **Figure 3**. The BC-converted carbon nanofibers are smooth and continuous (Figure 3A), while the LRF decoration renders the BC–LRF carbon nanofibers wavy and rough (Figure 3B). High magnification TEM (Figure 3C) shows highly ordered graphitic carbon and the selected area electron diffraction (SAED) of the two carbon aerogels display the patterns resembling those of single crystals of AB Bernal-stacked graphite (Figure 3D,E).[27] Diffraction spot streaking and additional diffraction spots on the patterns can be caused by different reasons, including crystalline lattice distortion,[28] rotational stacking faults,[29] and overlapping domains.[30] The interlayer spacing in Figure 3C is measured to be 3.12 Å (Figure 3F), which is close to that of graphite.

2.3. Mechanical Properties of Hydrogels and Carbon Aerogels

Properties of the pristine BC hydrogel were first evaluated. The hydrogel contains large fraction of water (up to 99.5 wt%) and the water can be squeezed out of the gel without damaging the BC network. **Figure 4**A,B shows that the gel cube can be compressed from thickness 13.5 mm to 0.6 mm (a 96% compression ratio) and subsequently recovers to its original size after being immersed in water for over 2 h. This result indicates the outstanding strength/elasticity of the BC network and its strong capability to reversibly absorb/desorb liquids under mechanical stresses. Such a property is not obtainable by many traditional polymer hydrogels (e.g., polyvinyl alcohol hydrogel), where the absorbed liquids cannot be pressed out without rupturing the gels due to weak gel network and/or overly strong water–polymer bonding. This unique property of the BC gel allows convenient liquid impregnation for different application purposes.

Carbonization of the aerogels reduces their volumes. The volumes of pure BC and BC–LRF carbon aerogels are 20% and 67% of their corresponding aerogels (Figure 4C,D). The lower shrinkage rate for BC–LRF is due to the filling of the LRF nanoaggregates that are coated on the BC nanofiber's surfaces. As a

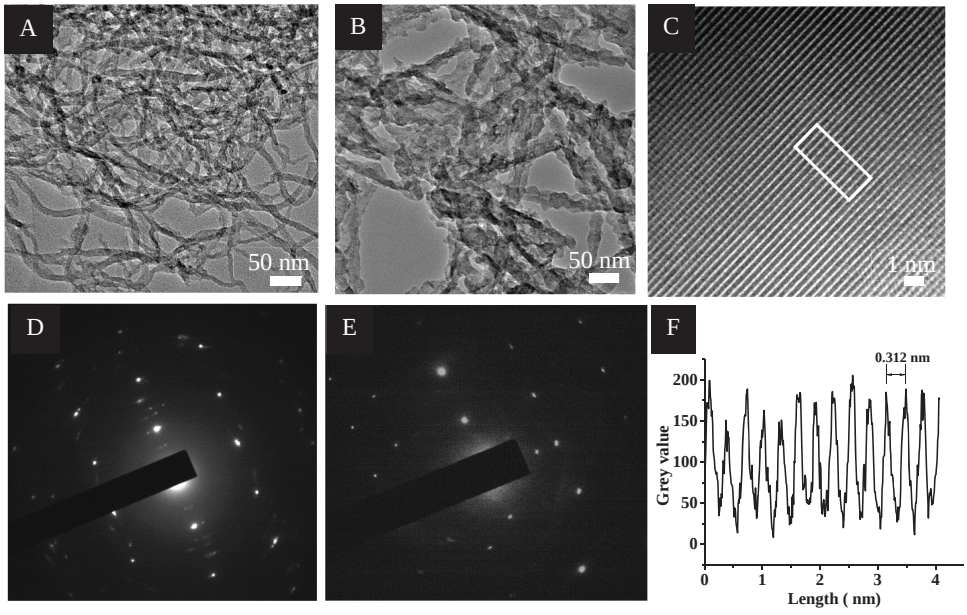

Figure 3. A) TEM image of BC carbon aerogel; B) TEM image of BC–LRF16 carbon aerogel; C) high magnification of TEM image of BC carbon aerogel; D,E) SAED of BC carbon aerogel and BC–LRF16 carbon aerogel; F) intensity profile taken by the box in (C).

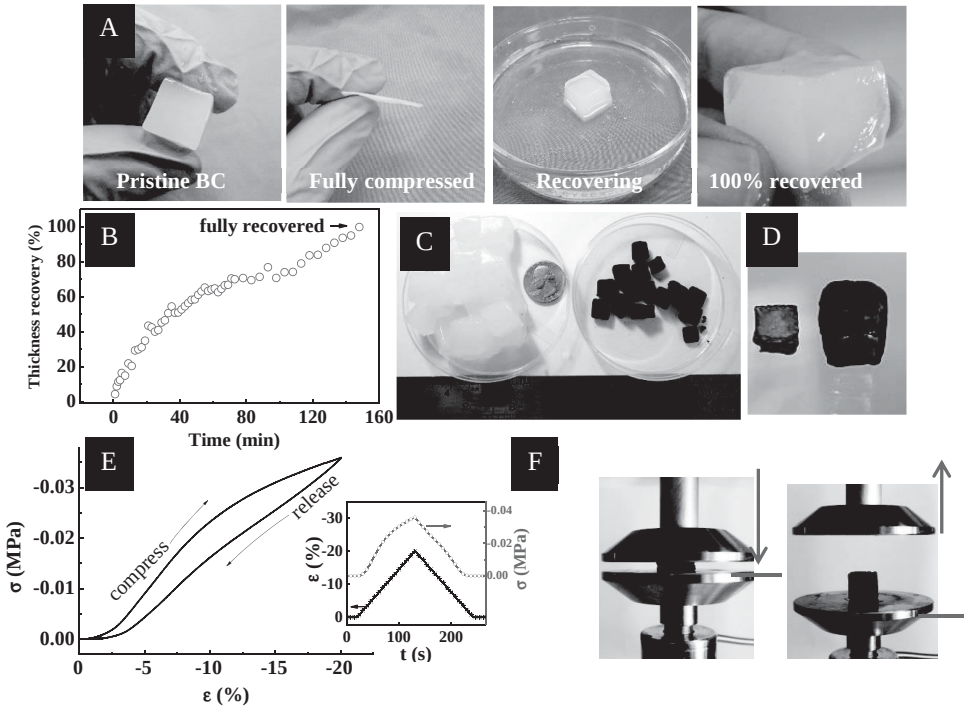

Figure 4. A) Shape recovery of pristine BC hydrogels; B) thickness recovery versus time for the hydrogel after being immersed in water; C) comparison of BC hydrogels and BC–LRF carbon aerogels; D) comparison between BC carbon aerogel and BC–LRF carbon aerogel; E) representative compression test curve of BC–LRF16 carbon aerogels; the inset shows the stain and stress profiles; F) reversible deformation of the BC–LRF carbon aerogel under 20% strain.

result, the density of the BC–LRF16 carbon aerogel increases to ≈0.026 g cm^{-3} from ≈0.013 g cm^{-3} of the pure BC carbon aerogel. These densities compare favorably to that of the carbon aerogel made from watermelon (0.058 g cm^{-3}).[31] Figure 4E shows the stress–strain curve for the BC–LRF16 carbon aerogel under cyclic compression at a maximum strain of 20%. A maximum stress of 0.03 MPa and a Young's modulus of ≈0.328 MPa were achieved, which are comparable to previously reported values.[31] The moduli of carbon aerogels are often low and vary significantly depending on their densities.[32,33] Nardecchia et al. have shown a modulus range between 0.05 and 29 MPa for different carbon aerogels.[34] The stress–strain curve in Figure 4E and the picture in Figure 4F show that the carbon aerogel can undergo at least 20% reversible deformation. The weak hysteresis loop suggests that part of the mechanical energy is dissipated during the deformation. Traditional RF and LRF carbon aerogels are brittle and fragile.[35] The discovery made here to significantly toughen these aerogels using BC nanofiber network removes a serious drawback of the materials and expands their applications.

2.4. Surface Area and Porosity of BC–LRF Carbon Aerogels

Representative N_2 adsorption–desorption isotherms of the carbon aerogels are shown in **Figure 5**A. The initial volume jump

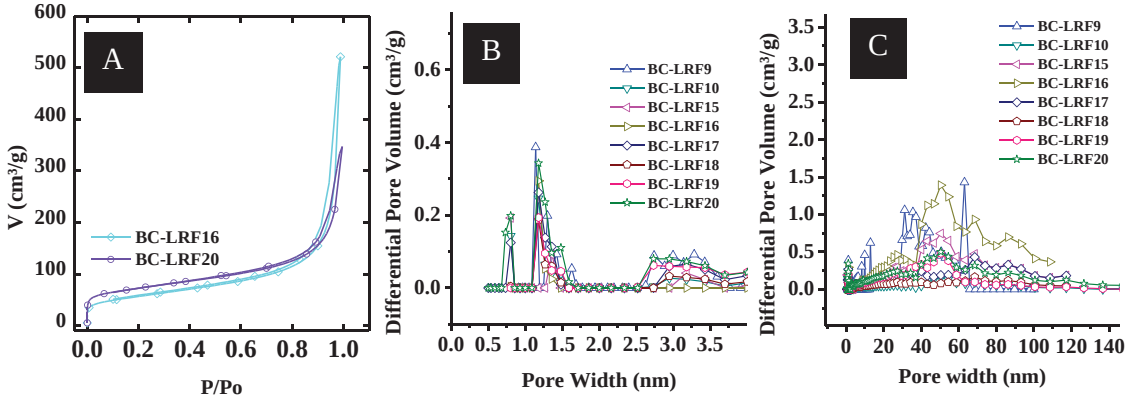

Figure 5. A) Representative N_2 adsorption–desorption isotherms; B) pore size distributions of the BC–LRF carbon aerogels; and C) the same pore size distributions within a smaller size range.

Table 2. Surface area and pore size for BC–LRF carbon aerogels.

Sample	SSA_{total} [$m^2 g^{-1}$]	SSA_{micro} [$m^2 g^{-1}$]	SSA_{meso} [$m^2 g^{-1}$]	SSA_{micro}/SSA_{total} [%]	SSA_{meso}/SSA_{total} [%]	Mean pore width [nm]
BC–LRF9	88.5	8.0	62.8	9	71	18.9
BC–LRF10	111.1	16.5	92.2	15	83	8.5
BC–LRF15	191.8	10.0	163.0	5	85	13.5
BC–LRF16	199.4	11.7	157.5	6	79	17.8
BC–LRF17	215.3	17.4	187.3	8	87	10.0
BC–LRF18	109.5	9.1	99.6	8	91	9.4
BC–LRF19	117.6	7.1	109.4	6	93	11.1
BC–LRF20	250.5	24.4	200.4	10	80	10.2

at near zero P/P_0, the plateau for $0 < P/P_0 < 0.8$ and the hysteresis, and the rapid increase at high P/P_0 indicate the presence of micropores (<2 nm), mesopores (2–50 nm), and macropores (>50 nm) in the aerogels, respectively.[36,37] Based on the isotherms, the total specific surface area (SSA_{total}), specific surface areas of micropores (SSA_{micro}) and mesopores (SSA_{meso}), and average pore width of the carbon aerogels were calculated using Barrett–Joyner–Halenda (BJH) and the density functional theory (DFT). The results are summarized in **Table 2**. SSA_{total} of the BC–LRF carbon aerogels ranges between 82 and 250 $m^2 g^{-1}$. Their average pore width varies between 8.5 nm and 19.8 nm, indicating that the majority of the pores are mesopores. Indeed, mesopores account for 71%–93% of the total surface area as indicated by the SSA_{meso}/SSA_{total} values in Table 2. This pore size distribution can also be recognized from Figure 5B, where the peaks for mesopores largely dominate the chart. Within the micropore size range, Figure 5C does show that most of the micropores have a width of ≈0.75 nm or ≈1.25 nm. The dominant mesopores in the carbon aerogels are most likely inherited from their precursor aerogels, which are produced by CO_2 supercrical drying. Organic aerogels produced using this method have been shown to comprise mainly mesopores: 10.5–28.9 nm in lignocellulose aerogels,[13] 20–40 nm in soy–tannin aerogels,[38] and 15–30 nm in LRF aerogels.[12] The high population of mesopores is attributed to the low surface tension at the supercritical CO_2/hydrogel interface, which hinders the agglomeration of the hydrogel networks when the CO_2 is extracted. The SSA of the aerogels in this study is relatively small compared to many other studies, which can be attributed to their high percentage of mesopores (rather than micropores) and the marked presence of macropores. The lack of micropores in these carbon aerogels is understandable because they do not undergo the acid or alkali assisted high temperature activation process, which is most commonly used to produce carbon materials with extremely high SSA.[36,39] In the following sections, the electrochemical properties of the carbon aerogels are studied and BC–LRF16 is chosen as a representative sample for discussion.

2.5. Functionalization and Dispersion of BC–LRF Carbon Aerogels

Functionalization by nitric acid (HNO_3) oxidation followed by sodium hydroxide (NaOH) neutralization has been used to increase the wettability of carbon materials and electrodes,[40,41] which can improve the dispersion of the carbon in electrode fabrication and increase the contact between the electrolytes and electrodes in use. FTIR spectra for the pristine and HNO_3–NaOH treated carbon aerogels are compared in **Figure 6**A, where the pristine carbon aerogel shows a C=C stretch at 1571 cm^{-1} of the graphite[42] and the treated one exhibits an additional peak at 1709 cm^{-1} due to the C=O stretch of the added —COOH after HNO_3 oxidation.[30,40] The X-ray photoelectron spectroscopy (XPS) spectra of the two samples are compared in Figure 6B. Three peaks located at 975.3, 532.3, and 284.5 eV for oxygen (KLL Auger transition and 1s) and carbon (1s) can be identified on both spectra.[31] The peak intensity ratios of O1s:C1s are 0.20 and 0.44 for the untreated and treated samples, respectively, which suggests more oxygen element on the treated sample surface. The existence of the weak oxygen peaks on the pristine carbon aerogel indicates remaining noncarbon sites on the carbon aerogels. A higher carbonization temperature and/or longer carbonization time may eliminate most of them.

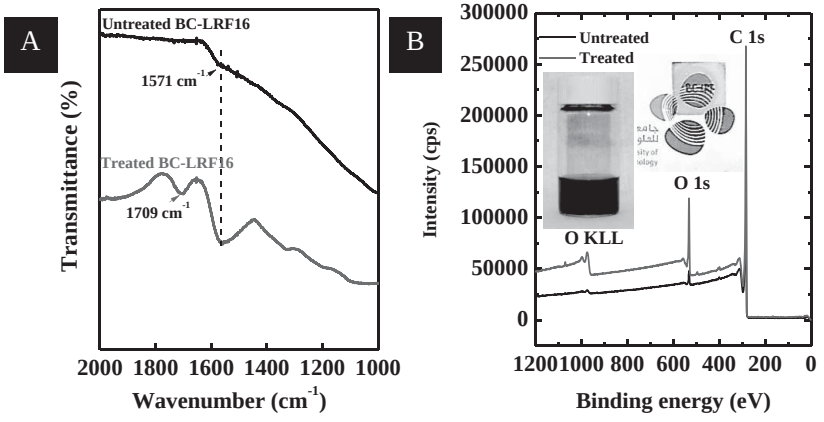

Figure 6. A) FTIR spectra of the pristine and HNO_3–NaOH treated BC–LRF16 carbon aerogels. B) XPS spectra of the two carbon aerogels. The insets show a stable dispersion of the treated BC–LRF16/acetylene black/PTFE (85:10:5) in ethanol (left) and the spin-coated film of the dispersion on a glass slide (right).

To confirm that the treated aerogel shows better dispersion in electrode fabrication, the ground BC–LRF16 carbon aerogel, acetylene black, and polytetrafluoroethylene (85:10:5) were dispersed in ethanol. The dispersion containing the treated BC–LRF16 remained stable without aggregation and precipitation after 48 h (Figure 6B, inset), whereas the dispersion containing the pristine carbon aerogel could not even be well dispersed (not shown). The stable dispersion could form highly transparent film on a glass slide via spin coating, indicating again the effect of the treatment.

2.6. Electrochemical Properties of BC–LRF Carbon Aerogels

The electrochemical performances of the BC–LRF16 carbon aerogel based electrodes were measured in 6 M potassium hydroxide (KOH) using a three-electrode configuration. In **Figure 7**A, the near-rectangular shape of the cyclic voltammograms is well maintained at a scan rate up to 25 mV s^{-1}. The galvanostatic charge/discharge (GCD) plots exhibit a triangular shape with a small internal resistance (Figure 7B). The curvature shown on the lines may suggest a certain degree of pseudocapacitive behavior of the electrode due to the existence of the oxygen-containing groups as revealed in the FTIR and XPS results.[36,43] The specific capacitances were calculated based on the GCD plots and the results are present in Figure 7C. The electrode shows specific capacitances of 124 and 107 F g^{-1} at scan rates of 0.5 and 1 A g^{-1}, respectively (as a comparison, the BC–LRF16 without acid treatment exhibits a capacitance of 35 F g^{-1} at 0.5 A g^{-1}). The contributions to these capacitances from the Ni foam current collector were found to be very small (see Figure S1, Supporting Information). The electrode also exhibits outstanding cycle stability—98% capacity retention after 10 000 charge–discharge cycles (Figure 7C, inset). The intersection of a Nyquist plot with the real axis indicates the equivalent series resistance (ESR) of an electrode. The ESR for BC–LRF16 is only ≈0.3 Ω (Figure 7D, inset), suggesting good conductivity and high quality of the electrode.[36,43] The negligible semi-circle on the plot indicates good electrode contact and high charge transfer rate at the electrode/electrolyte interface,[36,44] which can be partially attributed to the high wettability of the HNO_3 treated carbon aerogel.

2.7. High Areal Capacitance of BC–LRF Carbon Aerogels

The surface area available for electrolyte ion adsorption (i.e., effective surface area) and the charge separation distance are the two main factors determining the capacitance of electrical double-layer capacitors (EDLCs). Increasing the effective surface area through creating hierarchical nanostructured electrodes represents a major method to improve capacitor performance. Both experimental results and theoretical modeling have shown that, while the increase in the average diameter of mesopores

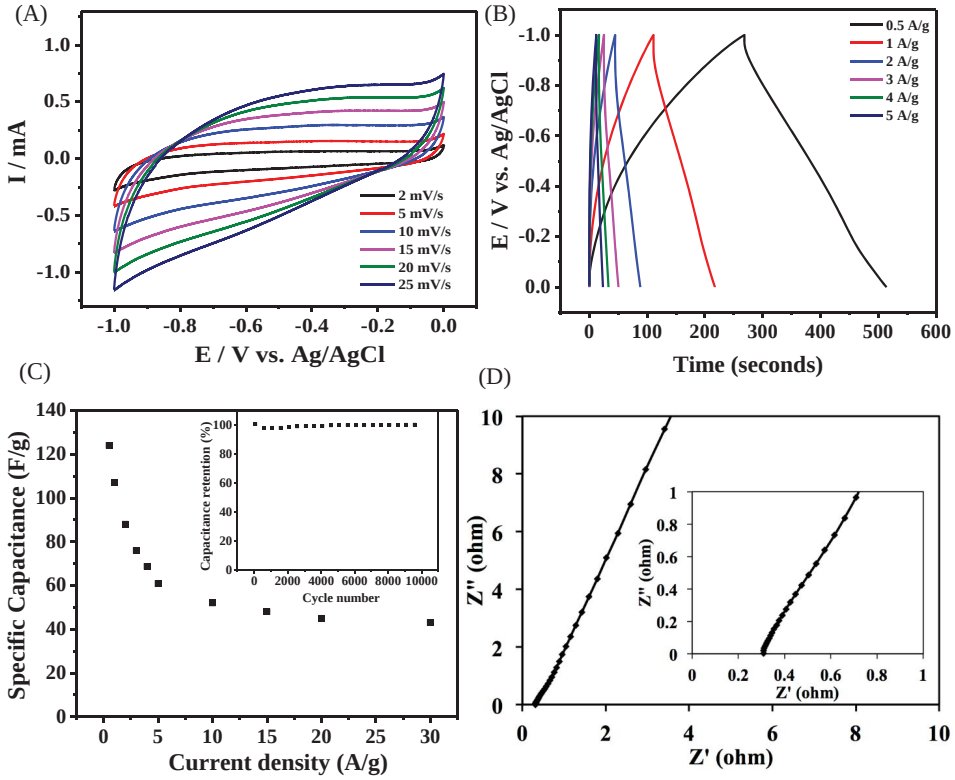

Figure 7. Electrochemical characteristics of BC–LRF16 carbon aerogel based electrodes. A) Cyclic voltammetry plots between 2 and 50 mV s^{-1}. B) Galvanostatic charge–discharge curves at various current densities. C) Specific capacitance as a function of current density. The inset shows capacitance retention under repeated charge–discharge. D) Nyquist plots (inset is the expanded view at high frequencies).

moderately improves the specific capacitance of an electrode, significant capacitance increases can be produced by the micropores less than 1 nm (about the size of electrolyte ions).[45–47] To obtain extremely high specific capacitance, there have to be abundant micropores for efficient ion trapping and adequate amount of mesopores serving as ion transportation pathways. The mesopores, while also trapping the ions and contributing to the capacitance, are important to the rate capability of the electrode by providing fast ion transportation. As shown by the N_2 adsorption–desorption results, mesopores are the primary pores in the BC–LRF carbon aerogels, which explains the electrode's moderate specific capacitance and the fast charge transfer shown by the Nyquist plot. The dominant role of the mesopores also exhibits the specific capacitance–SSA_{meso} relationship (**Figure 8**), which shows that the capacitance increases almost proportionally with the SSA_{meso}.

The areal capacitance, defined as capacitance/surface area, is an important parameter to evaluate the effectiveness of the surface area of an electrode for charge storage.[48] The areal capacitances calculated using the total surface area (C_{total}) and the mesopore surface area (C_{meso}) are listed in **Table 3** for the BC–LRF carbon aerogels. The values reported on other carbon materials are also given in this table and Table S1, Supporting Information, for comparison. BC–LRF16 exhibits a C_{total} and a C_{meso} of 62.2 and 78.7 μF cm^{-2}, respectively, much higher than the C_{total} of titanium carbide-derived carbon (13 μF cm^{-2})[45] and graphene (19 μF cm^{-2}),[49] which possess large total surface areas (1000 and 1310 m^2 g^{-1}, respectively). Two recent articles show that KOH activated graphene with a specific surface area between 3100 and 3290 m^2 g^{-1} only exhibits a specific capacitance of 160–174 F g^{-1} (≈5.3 μF cm^{-2}).[39,50] Microbead-based activated carbon shows a specific capacitance of 100 F g^{-1} (4.7 μF cm^{-2}) at 2130 m^2 g^{-1} specific surface area.[51] The much higher areal capacitance achieved in this study indicates that the BC–LRF carbon areogels have adequate mesopore/micropore ratios and good inter-pore connections that allow high level utilization of the surface areas. The aforementioned "high surface area, low capacitance" carbon materials possess abundant micropores that may not be sufficiently supplied with electrolyte ions through well connected mesopores during charge–discharge processes.

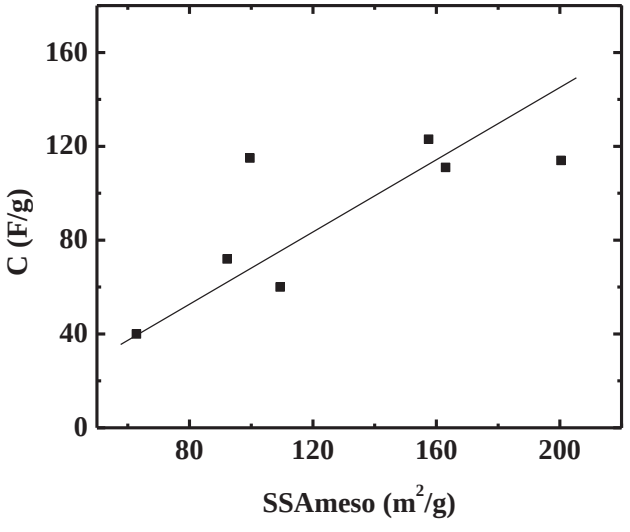

Figure 8. Specific capacitance as a function of mesopore surface area for the BC–LRF carbon aerogels.

Table 3. Areal capacitance of the BC–LRF aerogels.

Sample	$C_{gravimetric}$ [F g^{-1}]	C_{total} [μF cm^{-2}]	C_{meso} [μF cm^{-2}]	SSA_{total} [m^2 g^{-1}]
BC–LRF9	40	45.2	63.7	88.5
BC–LRF10	72	64.8	78.1	111.1
BC–LRF15	114	59.4	69.9	191.8
BC–LRF16	124	62.2	78.7	199.4
BC–LRF17	111	51.6	59.3	215.3
BC–LRF18	60	54.8	60.2	109.5
BC–LRF19	60	51.0	54.8	117.6
BC–LRF20	115	45.9	57.4	250.5
Activated carbon[51]	100	4.7	–	2130
Graphene[50]	160	5.2	–	3100
Graphene[39]	174	5.3	–	3290
Carbide-derived carbon[52]	140	13	–	80
Graphene[5]	128	18.2	–	–
Graphene[6]	247	19	–	–

Carbon aerogels have important applications in environmental remedies such as oil and dye removal due to their large surface area and superhydrophobicity.[34,53] Toughness is important for the carbon materials in these applications because mechanical forces are used when the materials are deployed, pressed to release adsorbates, and prepared for reuse. Lignin based carbon aerogels are fragile and hence restrained in these (and broader) applications. Toughening them using BC opens an innovative avenue to improve their handling and therefore can expand their applications.

Energy storage is another key application area of carbon materials. A wide array of carbon, including sphere-like activated carbon particulates (based on different carbon sources), electrospun nanofiber-converted carbon nanofibers,[54] 3D-architectured carbon areogels based on CNTs and graphene,[34] watermelon-based carbon areogel,[31] and others,[55] have been used as electrode materials in supercapacitors. The BC–LRF carbon aerogels developed in this study represent a new category of biomass-based carbon materials suitable for supercapacitor electrode use. The process used is facile, catalyst-free, and cost-effective. The products are high-purity CNT-like carbon fibers and fiber networks (areogels) containing high percentage of mesopores. Their high areal capacitance makes them promising electrode materials for supercapacitors. The specific capacitance of the carbon areogels can be further improved through commonly used carbon activation methods (acid, alkaline, or steam) to increase the micropore volume.

3. Conclusion

In this work, we report a facile methodology to synthesize catalyst-free, flexible, mesoporous, and highly graphitized carbon

aerogels based on bacterial cellulose toughened LRF gels. The carbon aerogels consist of core–shell structured carbon nanofibers, where the core and shell are graphitized BC nanofibers and LRF nanoaggregates, respectively. We show for the first time that large reversible deformations in BC–LRF carbon aerogels are attainable by utilizing the toughening effect of the BC nanofiber network. The unique blackberry-like structure and large mesopore concentration of these materials facilitate ion transportation and adsorption and lead to their high areal capacitance. Some of the potential applications of the carbon aerogels include oil/water separation, supercapacitors, batteries, catalyst supports, and sensors.

4. Experimental Section

Materials and BC–LRF Hydrogel Preparation: Alkali lignin ($M_w = 10\,000$), resorcinol (>99%), and formaldehyde (37% aqueous solution) were purchased from Sigma-Aldrich. Nitric acid (70%) was purchased from EMD and sodium hydroxide from ACROS. All the chemicals were used as received. BC gel cubes were produced by Thai Agri Foods Public Company. The cubes were cleaned by soaking in distilled water for 15 d and the water was changed every 24 h. The cleaned gel had a BC concentration of 0.5%. To prepare LRF hydrogels, lignin, resorcinol, formaldehyde, and sodium carbonate were added in 0.25 M sodium hydroxide to obtain a solution. The total concentration of the lignin, resorcinol, and formaldehyde in the solution was maintained at 10 wt% and the concentration of the sodium carbonate was fixed at 0.05 wt%. The weight ratio between the lignin, resorcinol, and formaldehyde (i.e., L:R:F) was varied and the tested ratios are listed in **Table** 4. LRF hydrogels were obtained after the solutions were kept at 80 °C for 48 h. To produce BC–LRF hydrogels, the cleaned BC gel cubes (≈8.25 g) were impregnated with the LRF gel precursors by immersing the cubes in the solutions. Sonication was applied to accelerate the impregnation process. The same condition was used to gel the LRF precursor inside the BC cubes.

Table 4. Formulation of BC–LRF hydrogels.

Sample	BC gel [g]	Lignin [g]	Resorcinol [g]	Formaldehyde [g]	Lignin content in LRF [wt%]	LRF gelation
BC–LRF1	8.25	0.2	0.2	3.2	6	No
BC–LRF 2	8.25	0.4	0.2	2.8	12	No
BC–LRF 3	8.25	0.6	0.2	2.4	19	No
BC–LRF 4	8.25	0.8	0.2	2.0	27	No
BC–LRF 5	8.25	1.2	0.2	1.2	46	No
BC–LRF 6	8.25	1.6	0.2	0.4	73	No
BC–LRF 7	8.25	1.0	1.0	0.4	42	No
BC–LRF 8	8.25	0.2	1.8	0.4	8	No
BC–LRF 9	8.25	0.2	1.2	1.2	7	Yes
BC–LRF 10	8.25	0.2	0.8	2.4	6	Yes
BC–LRF 11	8.25	0.4	0.4	2.4	13	No
BC–LRF 12	8.25	0.8	0.4	1.6	29	No
BC–LRF 13	8.25	1.2	0.4	0.8	50	No
BC–LRF 14	8.25	1.0	0.6	0.8	42	No
BC–LRF 15	8.25	0.8	0.8	0.8	33	Yes
BC–LRF 16	8.25	0.4	1.2	0.8	17	Yes
BC–LRF 17	8.25	0.4	0.8	1.6	14	Yes
BC–LRF 18	8.25	0.6	0.6	1.6	21	Yes
BC–LRF 19	8.25	0.8	0.6	1.2	31	Yes
BC–LRF 20	8.25	0.6	0.8	1.2	23	Yes

Preparation of BC–LRF Carbon Aerogel: The BC–LRF hydrogels were converted to aerogels by CO_2 supercritical drying. The hydrogels first underwent solvent exchange to replace their contained water with ethanol and then were put in a custom-built supercritical dryer. The dryer was immediately filled with 600 mL ethanol, which was gradually exchanged with liquid CO_2 (bone dry, Airgas) according to the following steps. 600 mL liquid CO_2 was added to the dryer and the pressure was increased to 5.5 MPa, while maintaining the temperature at 15 °C. The dryer was drained after 4 h and a fresh amount of liquid CO_2 was added. This rinse process was repeated ≈15 times to make sure all ethanol was removed. After that, the temperature and pressure were raised to 65 °C and 8.3 MPa above the critical point for CO_2 (31.1 °C and 7.39 MPa), and the conditions were maintained for 30 min. Finally, the chamber was slowly depressurized at a controlled rate (≈100 kPa min^{-1}) and the BC–LRF aerogels were obtained. Carbonization of the aerogels was conducted using an Atomate 110 horizontal tube furnace. The process included a sequence of steps: 30–500 °C temperature ramp at 10 °C min^{-1}, 100 min isothermal holding, 500–1000 °C ramp at 20 °C min^{-1}, and finally 60 min isothermal holding. 200 sccm argon flow was supplied during the whole process. To increase the wettability of the obtained carbon aerogels, the materials were treated using 70% nitric acid at 60 °C for 90 min and then washed with 0.2 M sodium hydroxide and distilled water thoroughly.

Characterization: A JEOL 7600 field-emission scanning electron microscopy (FE-SEM) operating at 2 kV was used to study the morphology of the obtained organic and carbon aerogels. TEM imaging was performed using a JEOL TEM-2100 equipped with a LaB6 emitter. To prepare the TEM samples, the carbon aerogel was dispersed in ethanol by mechanical stirring and a drop of the dispersion was placed on a 300-mesh Formvar-coated carbon film copper grid. Surface chemical bonding of the BC–LRF carbon aerogels was characterized by FTIR using a Nicolet 6700 spectrometer from Thermo Scientific. An average spectrum (4000 to 650 cm^{-1}) for each sample was obtained based on 32 repetitive scans. XPS spectra were obtained using a Kratos Axis Ultra XPS System. An ASAP2420 surface area and porosity system from Micrometritics was used to determine the surface areas and pore sizes of the organic and carbon aerogels. To study the electrochemical properties of the BC–LRF carbon aerogels, the aerogels (85 wt%), polytetrafluoroethylene (PTFE) (10 wt%), and acetylene black (5 wt%) were mixed in ethanol by sonication for 30 min to obtain stable dispersions. Electrodes were prepared by coating Ni foam with the dispersions and by allowing them to dry at 60 °C for 12 h. The mass loading of the materials is about 2–3 mg cm^{-2}. Electrochemical tests were performed using a Biologic VMP3 workstation and a three-electrode configuration with the carbon aerogel as the working electrode, Ag/AgCl as the reference electrode, and a platinum wire as the counter electrode. The 6 M aqueous KOH solution was used as the electrolyte. Cyclic voltammetry tests were conducted at different potential scan rates (2–25 mV s^{-1}) between −1 and 0 V. Galvanostatic charge/discharge experiments were performed using current densities between 0.5 and 5 A g^{-1}. The specific gravimetric capacitances were calculated from the discharge curves using the equation $C = (I\Delta t)/(m\Delta V)$, where I is the constant discharge current (A), Δt is the discharge time (s), ΔV is the discharge voltage excluding the IR drop (V), and m is the mass of the active materials. Bare Ni foam was also tested using the identical conditions to estimate its contribution to the capacitance. Electrochemical impedance spectroscopy (EIS) was conducted within the frequency range between 100 kHz and 0.01 Hz.

Supporting Information

Supporting Information is available from the Wiley Online Library or from the author.

Acknowledgements

X.X. and J.Z. contributed equally to this work. Financial supports from ND NASA EPSCoR and KAUST Baseline are greatly appreciated. The authors are grateful to Mr. Xingyu Chen for his contribution to hydrogel synthesis and aerogel carbonization. The authors would also like to thank Asghar Rezaei for his assistance on the carbon aerogel compression test.

Received: February 8, 2015
Revised: March 22, 2015
Published online: April 15, 2015

[1] X. Dong, H. Xu, X. Wang, Y. Huang, M. B. Chan-Park, H. Zhang, *ACS Nano* **2012**, 3206.
[2] F. Yavari, Z. Chen, A. V Thomas, W. Ren, H. M. Cheng, N. Koratkar, *Sci. Rep.* **2011**, *1*, 166.
[3] X. Gui, J. Wei, K. Wang, A. Cao, H. Zhu, Y. Jia, Q. Shu, D. Wu, *Adv. Mater.* **2010**, *22*, 617.
[4] Z. Wu, S. Yang, Y. Sun, K. Parvez, X. Feng, *J. Am. Chem. Soc.* **2012**, *134*, 9082.
[5] N. Zhao, Z. Wang, C. Cai, H. Shen, F. Liang, D. Wang, C. Wang, T. Zhu, J. Guo, Y. Wang, X. Liu, C. Duan, *Adv. Mater.* **2014**, *26*, 6994.
[6] L. Sun, C. Tian, M. Li, X. Meng, L. Wang, R. Wang, J. Yin, H. Fu, *J. Mater. Chem. A* **2013**, *1*, 6462.
[7] N. H. Phan, S. Rio, C. Faur, L. Le Coq, P. Le Cloirec, T. H. Nguyen, *Carbon* **2006**, *44*, 2569.
[8] C. Byrne, D. C. Nagle, *Carbon* **1997**, *35*, 267.
[9] H. Wang, Z. Xu, A. Kohandehghan, Z. Li, K. Cui, X. Tan, T. J. Stephenson, C. K. King, C. M. B. Holt, B. C. Olsen, J. K. Tak, D. Harfield, A. O. Anyia, D. Mitlin, *ACS Nano* **2013**, *7*, 5131.
[10] B. Wang, R. Karthikeyan, X. Y. Lu, J. Xuan, M. K. H. Leung, *Ind. Eng. Chem. Res.* **2013**, *52*, 18251.
[11] X. Xu, J. Zhou, L. Jiang, G. Lubineau, Y. Chen, X.-F. Wu, R. Piere, *Mater. Lett.* **2013**, *109*, 175.
[12] Z. Du, X. B. Sun, *Adv. Mater. Res. Mater. Res.* **2010**, *113-116*, 1837.
[13] Y. Lu, Q. Sun, D. Yang, X. She, X. Yao, G. Zhu, Y. Liu, H. Zhao, J. Li, *J. Mater. Chem.* **2012**, *22*, 13548.
[14] L. I. Grishechko, G. Amaral-Labat, A. Szczurek, V. Fierro, B. N. Kuznetsov, A. Celzard, *Microporous Mesoporous Mater.* **2013**, *168*, 19.
[15] L. I. Grishechko, G. Amaral-Labat, A. Szczurek, V. Fierro, B. N. Kuznetsov, A. Pizzi, A. Celzard, *Ind. Crops Prod.* **2013**, *41*, 347.
[16] R. Sescousse, A. Smacchia, T. Budtova, *Cellulose* **2010**, *17*, 1137.
[17] O. Aaltonen, O. Jauhiainen, *Carbohydr. Polym.* **2009**, *75*, 125.
[18] D. Zhang, L. Qi, *Chem. Commun.* **2005**, 2735.
[19] R. T. Olsson, M. A. S. Azizi Samir, G. Salazar-Alvarez, L. Belova, V. Ström, L. A. Berglund, O. Ikkala, J. Nogués, U. W. Gedde, *Nat. Nanotechnol.* **2010**, *5*, 584.
[20] Z. Y. Wu, C. Li, H.-W. Liang, J. F. Chen, S. H. Yu, *Angew. Chem. Int. Ed.* **2013**, *52*, 2925.
[21] J. Cai, S. Liu, J. Feng, S. Kimura, M. Wada, S. Kuga, L. Zhang, *Angew. Chem.* **2012**, *124*, 2118.
[22] J. Zou, J. Liu, A. S. Karakoti, A. Kumar, D. Joung, Q. Li, S. I. Khondaker, S. Seal, L. Zhai, *ACS Nano* **2010**, *4*, 7293.
[23] C. Xu, Z. Zhang, Y. Li, P. Gao, *ACS Nano* **2012**, *6*, 7103.
[24] H. Yamamoto, M. Amaike, H. Saitoh, Y. Sano, *Mater. Sci. Eng. C* **2000**, *7*, 143.
[25] M. C. Gutiérrez, F. Rubio, F. del Monte, *Chem. Mater.* **2010**, *22*, 2711.
[26] S. A. Al-Muhtaseb, J. A. Ritter, *Adv. Mater.* **2003**, *15*, 101.
[27] D. Geng, B. Wu, Y. Guo, L. Huang, Y. Xue, J. Chen, G. Yu, L. Jiang, W. Hu, Y. Liu, *Proc. Natl. Acad. Sci. U.S.A.* **2012**, *109*, 7992.
[28] C.-T. Pan, J. A. Hinks, Q. M. Ramasse, G. Greaves, U. Bangert, S. E. Donnelly, S. J. Haigh, *Sci. Rep.* **2014**, *4*, 6334.
[29] J. H. Warner, M. H. Ru, T. Gemming, B. Bu, G. A. D. Briggs, *Nano Lett.* **2009**, *9*, 102.
[30] X. Zhang, T. V Sreekumar, T. Liu, S. Kumar, *J. Phys. Chem. B* **2004**, *108*, 16435.
[31] X. Wu, T. Wen, H. Guo, S. Yang, X. Wang, A. Xu, *ACS Nano* **2013**.
[32] J. Zhou, G. Lubineau, *ACS Appl. Mater. Interfaces* **2013**, *5*, 6189.
[33] J. Zhou, Q. Gao, T. Fukawa, H. Shirai, M. Kimura, *Nanotechnology* **2011**, *22*, 275501.
[34] S. Nardecchia, D. Carriazo, M. L. Ferrer, M. C. Gutiérrez, F. del Monte, *Chem. Soc. Rev.* **2013**, *42*, 794.
[35] D. R. Anderson, M. L. Stroud, R. M. Rolison, *Nano Lett.* **2002**, *2*, 235.
[36] L. L. Zhang, X. Zhao, M. D. Stoller, Y. Zhu, H. Ji, S. Murali, Y. Wu, S. Perales, B. Clevenger, R. S. Ruoff, *Nano Lett.* **2012**, *12*, 1806.
[37] M. Kruk, M. Jaroniec, *Chem. Mater.* **2001**, *13*, 3169.
[38] G. Amaral-Labat, L. Grishechko, A. Szczurek, V. Fierro, A. Pizzi, B. Kuznetsov, A. Celzard, *Green Chem.* **2012**, *14*, 3099.
[39] T. Y. Kim, G. Jung, S. Yoo, K. S. Suh, R. S. Ruoff, *ACS Nano* **2013**, *7*, 6899.
[40] K. A. Worsley, I. Kalinina, E. Bekyarova, R. C. Haddon, *J. Am. Chem. Soc.* **2009**, *131*, 18153.
[41] A. G. Pandolfo, A. F. Hollenkamp, *J. Power Sources* **2006**, *157*, 11.
[42] M. A. Hamon, H. Hui, P. Bhowmik, H. M. E. Itkis, R. C. Haddon, *Appl. Phys. A* **2002**, *338*, 333.
[43] M. Zhi, F. Yang, F. Meng, M. Li, A. Manivannan, N. Wu, *ACS Sustain. Chem. Eng.* **2014**, *2*, 1592.
[44] C. Portet, M. A. Lillo-Ródenas, A. Linares-Solano, Y. Gogotsi, *Phys. Chem. Chem. Phys.* **2009**, *11*, 4943.
[45] J. Chmiola, G. Yushin, Y. Gogotsi, C. Portet, P. Simon, P. L. Taberna, *Science* **2006**, *313*, 1760.
[46] J. Huang, B. G. Sumpter, V. Meunier, *Chemistry* **2008**, *14*, 6614.
[47] J. Huang, B. G. Sumpter, V. Meunier, *Angew. Chem. Int. Ed.* **2008**, *47*, 520.
[48] E. Raymundo-Piñero, K. Kierzek, J. Machnikowski, F. Béguin, *Carbon* **2006**, *44*, 2498.
[49] J. J. Yoo, K. Balakrishnan, J. Huang, V. Meunier, B. G. Sumpter, A. Srivastava, M. Conway, A. L. M. Reddy, J. Yu, R. Vajtai, P. M. Ajayan, *Nano Lett.* **2011**, *11*, 1423.
[50] Y. Zhu, S. Murali, M. D. Stoller, K. J. Ganesh, W. Cai, P. J. Ferreira, A. Pirkle, R. M. Wallace, K.A Cychosz, M. Thommes, D. Su, E. A. Stach, R. S. Ruoff, *Science* **2011**, *332*, 1537.
[51] D. Qu, H. Shi, *J. Power Sources* **1998**, *74*, 99.
[52] C. Largeot, C. Portet, J. Chmiola, P. Taberna, Y. Gogotsi, P. Simon, *J. Am. Chem. Soc.* **2008**, *130*, 2730.
[53] H. Sun, Z. Xu, C. Gao, *Adv. Mater.* **2013**, *25*, 2554.
[54] M. Inagaki, Y. Yang, F. Kang, *Adv. Mater.* **2012**, *24*, 2547.
[55] P. Simon, Y. Gogotsi, *Nat. Mater.* **2008**, *7*, 845.